

# Quantification of reversible and irreversible lithium in practical lithium-metal batteries

Received: 29 January 2022

Accepted: 12 August 2022

Published online: 29 September 2022

 Check for updates

Wei Deng<sup>1,6</sup>, Xue Yin<sup>1,6</sup>, Wurigumula Bao<sup>2,6</sup>, Xufeng Zhou<sup>1,3</sup>✉, Zhiyuan Hu<sup>1</sup>,  
Bangyi He<sup>1</sup>, Bao Qiu<sup>1,3</sup>, Ying Shirley Meng<sup>2,4,5</sup>✉ and Zhaoping Liu<sup>1,3</sup>✉

Accurate assessment of the reversibility of electrodes is crucial for battery performance evaluations. However, it is challenging to acquire the true reversibility of the Li anode in lithium-metal batteries, mainly because an excessive amount of Li is commonly used. Here we propose an analytic approach to quantitatively evaluate the reversibility of practical lithium-metal batteries. We identify key parameters that govern the anode reversibility and subsequently establish their relationship with the cycle number by considering the mass of active and inactive Li of the cycled Li anode. Using this method, we show that the mass of active Li can be quantitatively distinguished from the mass of inactive Li of the cycled anodes in Amp hour-level pouch cells. This work opens an avenue for accurately assessing degradation and failure in lithium-metal batteries.

Lithium-metal batteries (LMBs)—whose energy densities potentially go beyond 500 Wh kg<sup>-1</sup>—are an important focus in the current battery technology development<sup>1–4</sup>. However, it remains a big challenge to distinguish reversible Li from the irreversible one in the cycled lithium-metal anode (LMA). This is vital for accurate evaluation of reversibility of practical LMBs<sup>5,6</sup>.

For anode-free cells without LMAs, the irreversible capacity loss can be easily identified by Coulombic inefficiency of the cell (CIE<sub>n</sub>, *n* is cycle number, defined in Fig. 1). An example of using CIE<sub>n</sub> to illustrate cell degradation is shown in Supplementary Figs. 1 and 2 (refs. <sup>7,8</sup>). Nevertheless, the degradation of excessive Li-containing LMBs mainly presents at the side of the LMA due to the much worse electrochemical irreversibility of LMAs than that of cathodes<sup>9–11</sup>. However, the LMA, as a Li reservoir, can continuously compensate for the loss of Li inventory in cathodes, which means that the CIE<sub>n</sub> of LMB does not precisely reflect the real irreversibility during cycling<sup>12–15</sup>. Therefore, quantitative parameters reflecting the true reversibility of LMAs should be established so as to objectively assess degradation behaviours of LMBs.

The irreversible Li species in a cycled LMA is composed of two parts, namely the (electro)chemically formed Li<sup>+</sup> compounds in the

solid electrolyte interphase (SEI-Li<sup>+</sup>) and electrically isolated metallic Li (inactive Li<sup>0</sup>)<sup>16,17</sup>. Such species, continuously formed and agglomerated during cycling, block the transport of both electrons and Li<sup>+</sup><sup>18,19</sup>, which, in turn, worsens the irreversibility of LMAs. Furthermore, a disproportionate cell balance (for example, a high N/P ratio, the ratio of anode capacity to cathode capacity) or/and a flooded electrolyte makes the irreversibility of LMA hard to be detected until extremely long cycling.

Herein we report an analytical methodology to quantitatively distinguish the active Li<sup>0</sup> from the inactive one in cycled LMAs in Ah-level LMB pouch cells. Biphenyl/tetrahydrofuran (THF) solution is employed to chemically metalate active Li<sup>0</sup> but also to preserve the completeness of SEI that encapsulates the inactive Li<sup>0</sup>. The as-separated active Li<sup>0</sup> and inactive Li<sup>0</sup> can be independently quantified. Furthermore, we identify key parameters, including the (ir)reversible percentage of plated Li from the cathode during a specific cycle, that describes the true (ir)reversibility of LMBs. The quantitative analysis based on the key parameters suggests that high stack pressure suppresses inherent Li loss by minimizing the cracking possibility of SEI, and agglomeration of dendritic Li under high charging rates drives the serious deterioration of the irreversibility. By using this analytical method—together

<sup>1</sup>Advanced Li-ion Battery Engineering Laboratory of Zhejiang Province, Key Laboratory of Graphene Technologies and Applications of Zhejiang Province and CAS Engineering Laboratory for Graphene, Ningbo Institute of Materials Technology & Engineering, Chinese Academy of Sciences (CAS), Zhejiang, P. R. China. <sup>2</sup>Department of NanoEngineering, University of California, San Diego, CA, USA. <sup>3</sup>Center of Materials Science and Optoelectronics Engineering, University of Chinese Academy of Sciences, Beijing, P. R. China. <sup>4</sup>Materials Science and Engineering, University of California, San Diego, CA, USA. <sup>5</sup>Pritzker School of Molecular Engineering, University of Chicago, Chicago, IL, USA. <sup>6</sup>These authors contributed equally: Wei Deng, Xue Yin, Wurigumula Bao. ✉e-mail: [zhouxf@nimte.ac.cn](mailto:zhouxf@nimte.ac.cn); [shirleymeng@uchicago.edu](mailto:shirleymeng@uchicago.edu); [liuzp@nimte.ac.cn](mailto:liuzp@nimte.ac.cn)

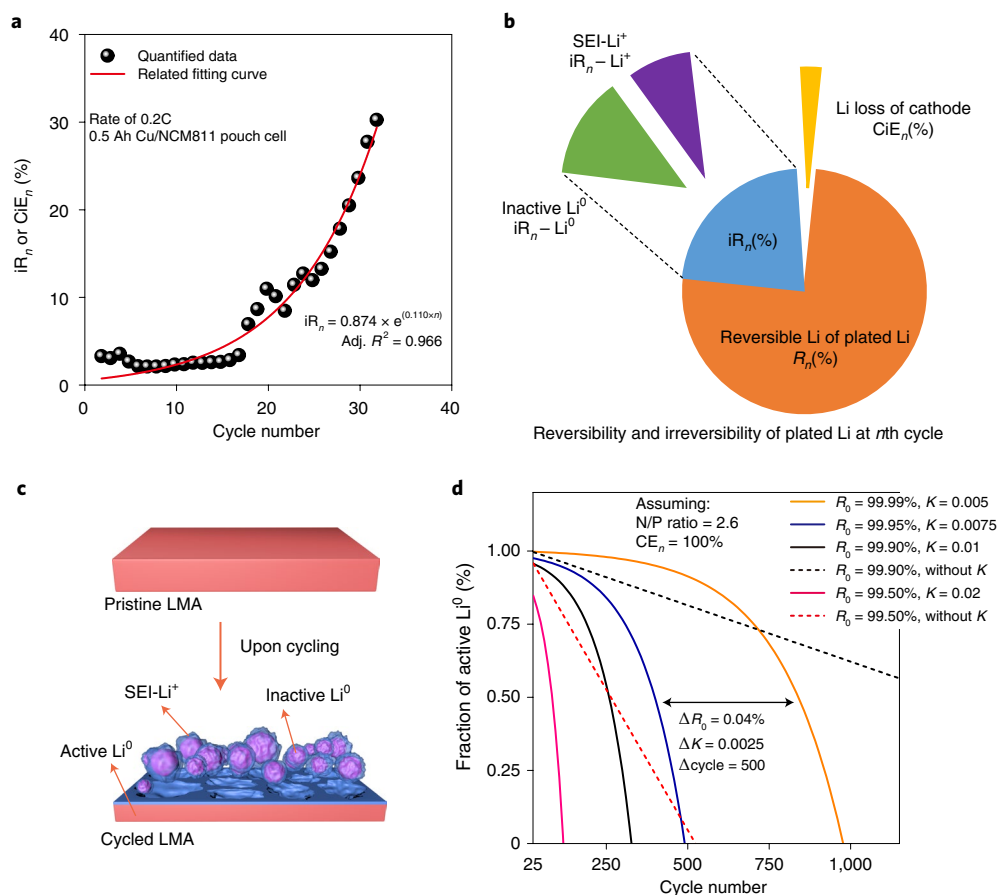


**Fig. 1 | Reversibility and irreversibility of a cycled LMA.** **a**, Coulombic inefficiency ( $CiE_n$ ,  $CiE_n = 100\% - CE_n$ ) versus cycle number ( $n$ ) of a 0.5 Ah Cu/NCM811 pouch cell that resembles an exponential growth pattern. Fitting of  $CiE_n$  within 33 cycles is based on equation (1), and the adjusted  $R^2$  (Adj.  $R^2$ ) equals 0.966.  $iR_n$ , irreversibility of anode-free pouch cells. **b**, The irreversible and reversible parts of plated Li in the LMA at the  $n$ th cycle, including  $CiE_n$ ,  $R_n$ ,  $iR_n(Li^0)$  and  $iR_n(Li^+)$ . **c**, Illustration of the composition and morphology of the LMA after

cycling. The porous irreversible Li layer above the residual active  $Li^0$  is composed of SEI-encapsulated inactive  $Li^0$ . **d**, The lifetime prediction of LMBs by applying constant irreversibility as the dashed line and variable irreversibility undergoing exponential growth ( $K$  as the growth coefficient) as the solid line.  $\Delta R_0$ ,  $\Delta K$  and  $\Delta cycle$  in **d** represent the difference of baseline reversibility, growth coefficient and cycle number, respectively, between the orange line and blue line. The N/P ratio of 2.6 is applied for Li/NCM811 pouch cells used in this work.

with qualitative morphology characterizations—the compositional and structural evolution of an LMA can be uncovered. Our quantification of reversible and irreversible Li provides a variable-independent way to study the effects of different operating conditions in LMBs, including stack pressures, charging/discharging rates, cut-off voltages and working temperatures. Our method also sheds light on effects of cell components including cathodes, anodes, binders, separator and electrolyte, which can make a substantial contribution to the LMB cell design.

### Key parameters for reversibility determination

According to the mathematical fitting of  $CiE_n$  versus cycle number ( $n$ ) of an anode-free pouch cell in Fig. 1a, the growth of the irreversible Li percentage (irreversibility,  $iR_n$ ) of the cell during charging/discharging is consistent with an exponential growth model. The fitting results demonstrate that the proportion of the irreversible Li loss in each cycle follows a time-variable exponential function closely related to the cycle number. In other words, the irreversible Li accumulated in earlier cycles will bring a proliferation of irreversibility in the later cycles<sup>20</sup>.

Due to similar Li plating/stripping behaviours between anode-free and LMA-containing cells, the irreversibility growth of LMAs in LMBs may follow the same model. As expressed in equation (1), a coefficient  $K$  is defined as the growth rate of  $iR_n$  based on an exponential growth model, which means the derivative of irreversibility growth

with respect to cycle number is proportional to the present irreversibility itself. Integration of equation (1) produces equation (2), which can be used to calculate the value of  $iR_n$ .  $iR_0$  in this equation means the inherent irreversibility determined by the cell system and external parameters, which is regarded as the baseline of the irreversibility of LMAs. The value of  $iR_0$  numerically equals the irreversibility of LMBs without considering the accumulation of irreversible Li.

$$\frac{d(iR_n)}{dn} = K \times iR_n \quad (1)$$

$$iR_n = iR_0 \times e^{K \times n} \quad (2)$$

During cycling, the Li ions extracted from the cathode transform into three parts, that is, the reversible Li re-intercalated into the cathode during discharging, the irreversible Li including SEI- $Li^+$  and inactive  $Li^0$  encapsulated by SEI and irreversible Li loss at the cathode side. The sum of the percentage of reversible Li ( $R_n$ ), irreversible Li ( $iR_n$ ) and irreversible Li loss of the cathode ( $CiE_n$ ) equals 100%, as expressed in equation (3). More specifically,  $R_n$  means the real reversibility of Li extracted from the cathode. Detailed meanings of the above parameters are also presented in Table 1 and Fig. 1b.

$$R_n + iR_n + CiE_n = 100\% \quad (3)$$

**Table 1 | The definition and relationship among key parameters to assess the reversibility of LMAs**

Item	Abbreviation	Definition
Reversibility and irreversibility parameters	$R_n$	Percentage of active $\text{Li}^0$ from plated Li at the $n$ th cycle <sup>a</sup>
	$iR_n(\text{Li}^0)$	Percentage of inactive $\text{Li}^0$ from plated Li at the $n$ th cycle
	$iR_n(\text{Li}^+)$	Percentage of irreversible SEI- $\text{Li}^+$ from plated Li at the $n$ th cycle
	$iR_n$	The sum percentage of $iR_n(\text{Li}^0)$ and $iR_n(\text{Li}^+)$ at the $n$ th cycle
	$K$	The growth coefficient of $iR_n$ , undergoing exponential growth
	$K(\text{Li}^0)$	The growth coefficient of $iR_n(\text{Li}^0)$ , undergoing exponential growth
Quantification parameters for calculation of (ir)reversibility parameters	$P$	Specific areal capacity of cathode ( $\text{mAh cm}^{-2}$ )
	$N$	Specific areal capacity of LMA ( $\text{mAh cm}^{-2}$ )
	$i\text{CE}_{\text{cell}}$	Initial Coulombic efficiency of the cell (equals to the initial Coulombic efficiency of the cathode)
	$\text{CE}_n$	Coulombic efficiency of LMB at the $n$ th cycle
	$\text{CiE}_n$	Coulombic inefficiency of LMB cell at the $n$ th cycle, equalling to the percentage of irreversible Li loss of the cathode at the $n$ th cycle
	$m_n$	Specific areal mass ( $\text{mg cm}^{-2}$ ) of active $\text{Li}^0$ in LMA at the $n$ th cycle
	$m_{\text{int}}$	Specific areal mass ( $\text{mg cm}^{-2}$ ) of initial LMA (before any electrochemical cycling)
	$m_n(iR\text{Li}^0)$	Specific areal mass of inactive $\text{Li}^0$ in LMA at the $n$ th cycle
	$n$	The specific cycle number

<sup>a</sup>When  $n=0$ ,  $iR_0$  and  $R_0$  are inherent parameters of the cell, which are determined by cycling conditions. These two parameters can be resolved by equations (5) and (3), respectively.

Thus, the determination of  $R_n$ ,  $iR_n$  and  $K$  is important to evaluate the reversibility and irreversibility of LMAs that are hidden beneath the Coulombic efficiency ( $\text{CE}_n$ ). However, these parameters cannot be directly quantified by simply calculating the total charge flows. As a cycled LMA is composed of active  $\text{Li}^0$ , SEI- $\text{Li}^+$  and inactive  $\text{Li}^0$  (Fig. 1c), quantifying active  $\text{Li}^0$  and inactive  $\text{Li}^0$  in an LMA is a prerequisite to decouple the reversible Li from the irreversible one<sup>8,14,17,21–25</sup>. There are two more obstacles to determine  $R_n$ ,  $iR_n$  and  $K$ . The first obstacle is how to separate active  $\text{Li}^0$  from inactive  $\text{Li}^0$  for independent identification of these species. Although inactive  $\text{Li}^0$  was quantified in anode-free coin cells by in situ nuclear magnetic resonance<sup>21,22,26–28</sup> and hydrogen titration gas chromatography<sup>17,29,30</sup>, these methods cannot distinguish active  $\text{Li}^0$  from inactive ones in a cycled LMA due to their identical metallic nature<sup>31</sup>. Another issue is how to establish the mathematical relationship between quantified mass, cycle number and irreversibility that can be used to determine the value of  $R_0$ ,  $iR_0$  and  $K$ .

### Calculation of key parameters

Here we first establish the relationship of  $R_0/iR_0/K$ , mass of Li and cycle number ( $n$ ), before deducing the reversibility of an LMB. More details on our analysis can be found in Methods and Fig. 2. An LMA as the Li reservoir can compensate for Li loss in every cycle to keep the cell capacity, which masks the true irreversibility. This irreversibility has

the cumulative effect that will eventually lead to the cell failure. Thus, we propose equation (4) to reveal the relation between Li reservoir amount and irreversibility.

According to the N/P ratio definition in LMB, the areal mass loading of Li from the cathode can be described by the initial areal mass loading of the LMA ( $m_{\text{int}}$ ,  $\text{mg cm}^{-2}$ ) divided by the value of the N/P ratio. Thus, the areal mass of residual active  $\text{Li}^0$  ( $m_n$ ) after  $n$  cycles is determined by  $iR_0$ ,  $K$  and the initial Coulombic efficiency of the cathode ( $i\text{CE}_{\text{cell}}$ ), which can be expressed in equation (4).

$$m_n = m_{\text{int}} - \frac{m_{\text{int}}}{N/P} \times i\text{CE}_{\text{cell}} \times iR_0 \times [e^{K \times 1} + e^{K \times 2} + \dots + e^{K \times n}] \quad (4)$$

As  $iR_0$  and  $K$  are regarded as constants for a specific cell, equation (4) can be simplified to equation (5), where the calculation of another constant,  $A_{\text{ir}}$ , follows equation (6).

$$m_n = m_{\text{int}} - A_{\text{ir}} \times e^{K \times n} \quad (5)$$

$$A_{\text{ir}} = \frac{m_{\text{int}} \times i\text{CE}_{\text{cell}} \times iR_0}{(N/P) \times K} \quad (6)$$

By fitting the mathematical relationship between  $m_n$  and  $n$  using equation (5), the value of  $K$  can be resolved, and  $iR_0$  can be determined using equation (6). Subsequently,  $iR_n$  can be acquired based on equation (2).

As shown in equation (3), knowing the value of  $iR_n$  enables the calculation for  $R_n$  because  $\text{CiE}_n$  can be directly measured from cycling tests.  $iR_n$  is composed of the irreversible percentage of SEI- $\text{Li}^+$  ( $iR_n(\text{Li}^+)$ ) and inactive  $\text{Li}^0$  ( $iR_n(\text{Li}^0)$ ) as expressed in equation (7), decoupling  $iR_n(\text{Li}^+)$  and  $iR_n(\text{Li}^0)$  from  $iR_n$  eventually accomplishes the goal to quantify irreversibility of the LMA.

$$iR_n = iR_n(\text{Li}^0) + iR_n(\text{Li}^+) \quad (7)$$

The irreversible percentage that is contributed by inactive  $\text{Li}^0$  at the  $n$ th cycles ( $iR_n(\text{Li}^0)$ ) is also regarded as following an exponential growth model with a growth coefficient as  $K(\text{Li}^0)$ . By fitting the mass of inactive  $\text{Li}^0$  after  $n$  cycles (as  $m_n(iR - \text{Li}^0)$ ) and  $n$  from quantification results using equation (8), we can calculate the value of  $iR_n(\text{Li}^0)$  through the exponential relationship between  $iR_0(\text{Li}^0)$  and  $K(\text{Li}^0)$  as expressed in equation (15) in Methods.

$$m_n(iR - \text{Li}^0) = \frac{iR_0(\text{Li}^0) \times m_{\text{int}}}{(N/P) \times K(\text{Li}^0)} \times e^{K(\text{Li}^0) \times n} \quad (8)$$

As long as the amount of the active  $\text{Li}^0$  and inactive  $\text{Li}^0$  can be quantified, it is possible to establish an index system composed of several key parameters (Table 1) such as  $R_0$ ,  $iR_0$ ,  $K$ ,  $iR_0(\text{Li}^0)$ ,  $K(\text{Li}^0)$  and  $iR_0(\text{Li}^+)$ . These parameters can be used to quantitatively describe the true reversibility of a practical LMB.

Assuming no capacity loss in the cathode upon cycling, failure predictions of LMBs are shown in Fig. 1d; the results demonstrate the significance of considering the proliferation effects of irreversibility. With same initial reversibility ( $R_0$ ), the lifetime of the cell is largely shortened by taking growth coefficient ( $K$ ) into consideration. The predicted lifetime is approximate to that of practical LMB pouch cells reported in previous works<sup>9,15,32,33</sup>, demonstrating the validity of this degradation model. When  $R_0$  is increased along with decreasing of  $K$ , the reversibility of LMB is evidently improved so that hundreds or even thousands of cycles could be achieved. A very small increment in  $R_0$  and/or decrement in  $K$  can cause huge differences in the cyclic stability. As previously mentioned, CE cannot be directly used to predict the cycle life. Either the SEI growth or the accumulation of inactive  $\text{Li}^0$  should be

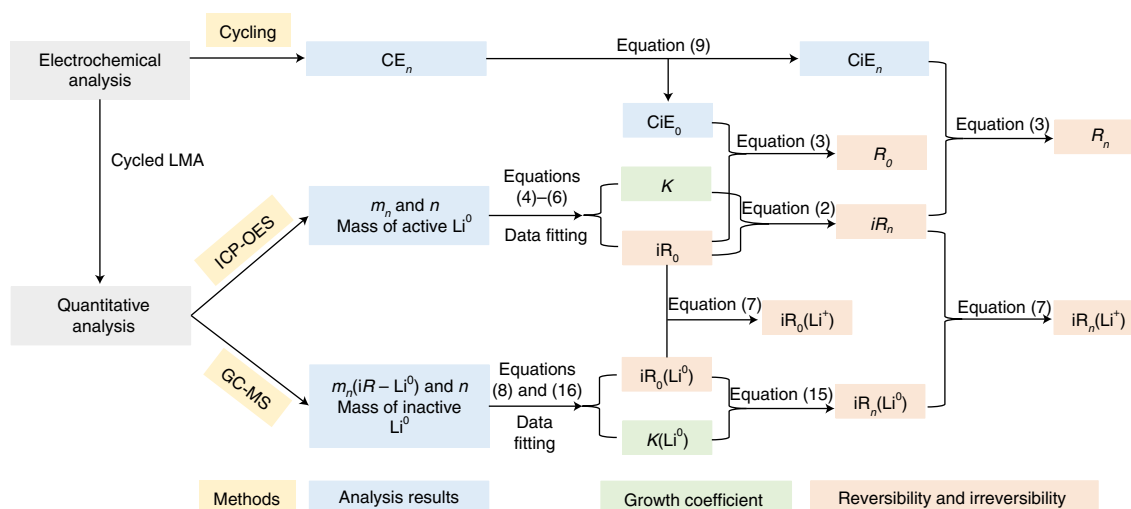


**Fig. 2 | The pathways for key parameter calculation.** Schematic of the relationship among key parameters and the calculation process based on the ICP-OES, H<sub>2</sub>-GCT (GC-MS) quantification results and cycling tests. Grey and

yellow represent type of analysis and methods of measurements, respectively. Blue, green and orange represent the analysis results, growth coefficients and parameters related to reversibility and irreversibility, respectively.

considered to have build-up effects on the degradation of LMB<sup>13</sup>. The requirements for  $R_0$  and  $K$  to reach specific cycle numbers are simulated in Supplementary Fig. 15b; knowing these parameters can predict the lifetime under certain conditions<sup>34</sup>. According to the principles of life prediction, if parameters such as  $K$  and  $R_0$  are optimized through regulations on cell components, a long lifetime of LMB can be achieved. As shown in the recently published results by the Battery500 Consortium with an optimized N/P ratio and electrolyte system, the life of LMB was extended to more than 600 cycles without a sudden capacity drop, implying a  $K$  value even smaller than 0.005 (the orange line in Fig. 1d) in this well-controlled LMB system<sup>15</sup>.

## Methodologies for quantifying active and inactive Li

Active Li<sup>0</sup>, inactive Li<sup>0</sup> and SEI-Li<sup>+</sup> are three major components in a cycled LMA (Fig. 3a). As active Li<sup>0</sup> and inactive Li<sup>0</sup> are both metallic lithium in terms of their composition, the only difference between them is that inactive Li<sup>0</sup> refers to the SEI-encapsulated particles<sup>35</sup>. Although the bulk Li foil is also covered by a SEI, punching an LMA to small pieces in an Ar-filled glove box for a quantitative analysis exposes the fresh surface of bulk Li. Considering the high chemical stability of SEI in organic solvents<sup>36,37</sup>, it is possible to chemically metalate<sup>38</sup> active Li<sup>0</sup> without dissolving SEI-protected inactive Li<sup>0</sup>.

Herein, a mixture of biphenyl and THF is used as a chemical metalation reagent. We start by examining the stability of the SEI (originated from carbonate-based electrolyte) in biphenyl/THF. First, the main inorganic salts (Li<sub>2</sub>CO<sub>3</sub>, LiF and LiOH) in the SEI are verified to be insoluble in biphenyl/THF (Supplementary Table 3 and Supplementary Note 2). Second, lithium ethylene dicarbonate, lithium methyl carbonate and lithium ethylene mono-carbonate are the main organic components of ethylene carbonate/ethyl methyl carbonate-derived SEI; lithium ethylene dicarbonate was reported to be directly synthesized from the chemical reaction between ethylene carbonate and lithium-naphthalenide<sup>36,37</sup>. Both aspects suggest the stability of inorganic and organic components in the SEI against biphenyl/THF and Li-biphenyl/THF. To directly confirm the stability of SEI-encapsulated inactive Li<sup>0</sup> in (Li-)biphenyl/THF, bare Li foil and anodes from anode-free pouch cells (Supplementary Fig. 8) and LMBs after cycling are immersed in biphenyl/THF. Figure 3b–d shows that no evident colour change of the solution containing only ‘dead Li’ on Cu foil (fully stripped anode from anode-free cells) is observed. This result is different from the dark colour of the solution containing either bare

Li or a cycled LMA, suggesting high chemical stability of the SEI. The digital photographs (Supplementary Fig. 9 and Supplementary Note 3) and inductively coupled plasma-optical emission spectrometer (ICP-OES) results (Supplementary Table 4) for the supernatants in Fig. 3b–d also demonstrate the stability of the SEI in (Li-)biphenyl/THF.

Detailed procedures for separating active Li<sup>0</sup> and inactive Li<sup>0</sup> are shown in Fig. 3e–g. Active Li<sup>0</sup> in cycled LMAs was firstly dissolved in biphenyl/THF (6.0 wt.% of biphenyl) and quantified by ICP-OES. Residual inactive Li<sup>0</sup> encapsulated by SEI was then reacted with deionized water. Hydrogen as the reaction product was collected and quickly injected to gas chromatography (GC) for quantifying the content of inactive Li<sup>0</sup> (termed as hydrogen gas chromatography titration, H<sub>2</sub>-GCT). The accuracy and sensitivity of ICP-OES and H<sub>2</sub>-GCT were measured before quantitative analysis. As shown in Fig. 3h, theoretical Li concentrations of standard biphenyl/THF solutions prepared by fully dissolving Li foils with pre-designed masses (Supplementary Fig. 10 and Supplementary Table 5) are linearly related to the measured concentrations from ICP-OES results, with goodness of fit approaching 1.00 ( $R^2 = 0.998$ ). To eliminate the interference of additional gases (CO<sub>2</sub>, CH<sub>4</sub>, C<sub>2</sub>H<sub>4</sub>, C<sub>2</sub>H<sub>6</sub>) from the reaction between SEI and water (Supplementary Figs. 11 and 12, Supplementary Table 6 and Supplementary Note 4) during H<sub>2</sub>-GCT measurement, a modified method for quantifying hydrogen was proposed by taking argon as the calibration component (Methods). In Fig. 3i, the baseline of H<sub>2</sub>-GCT shows a good linear relationship between the masses of pure Li and the peak area ratios of hydrogen to argon with  $R^2 = 0.993$ .

To further validate this method, we introduced the titration gas chromatography method<sup>17</sup> to measure the mass of metallic Li<sup>0</sup> (including inactive Li<sup>0</sup> and active Li<sup>0</sup>) in cycled LMAs, and the results (Supplementary Table 9 and Supplementary Note 8) are consistent with the sum of the separately quantified mass of inactive Li<sup>0</sup> and active Li<sup>0</sup> by this method. All these results confirm the accuracy of the analytical method we proposed in this work, guaranteeing quantitative and accurate analysis of active Li<sup>0</sup> and inactive Li<sup>0</sup> in cycled LMAs.

## Quantifying proportions of reversibility and irreversibility

To validate the efficacy of this methodology on practical LMBs, identical 0.5 Ah Li/NCM811 pouch cells operated under different stack pressures (100 kPa, 400 kPa, 800 kPa) and current rates (0.5C, 0.2C) were subjected to quantitative analysis. It is well acknowledged that external pressure can considerably affect the reversibility of LMAs<sup>7,32</sup>. The cycling

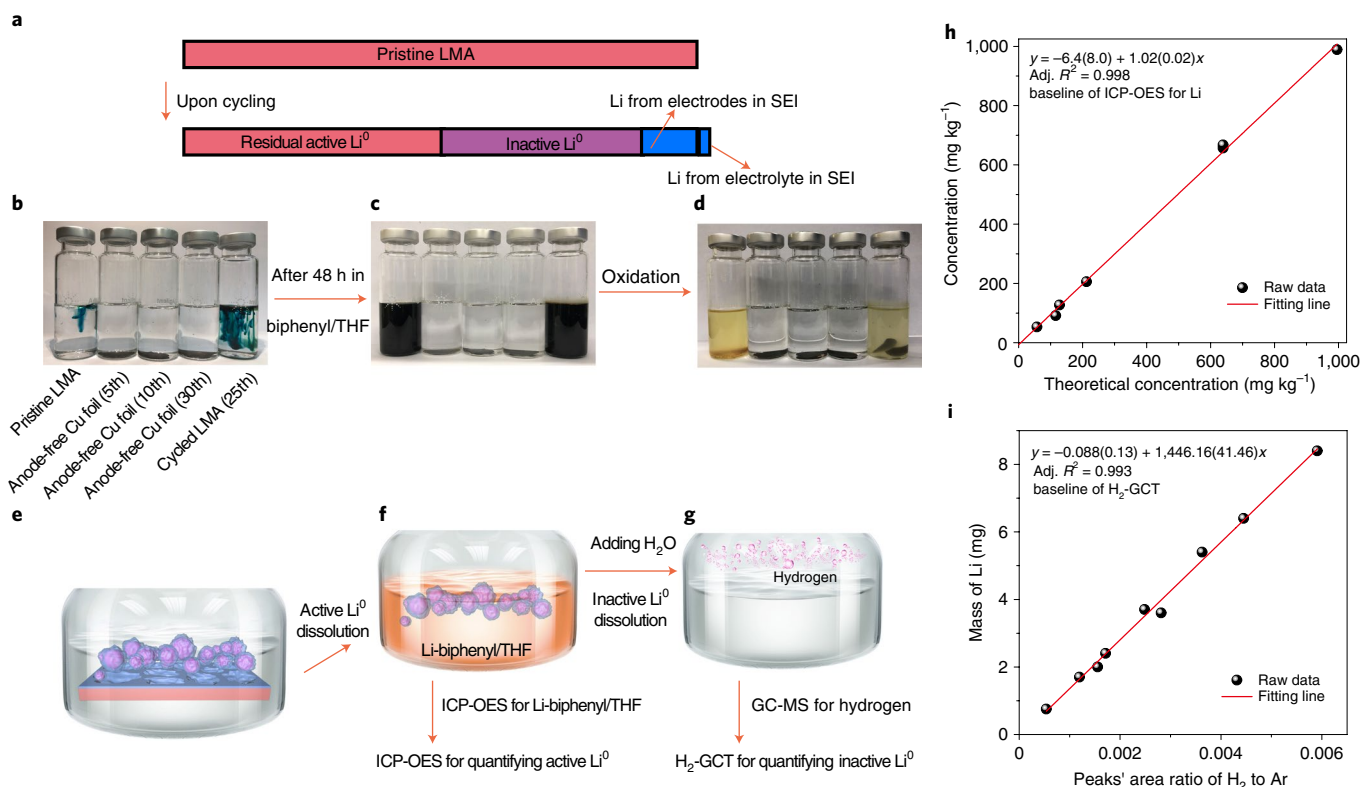


**Fig. 3 | Decoupling and quantifying inactive  $Li^0$  and active  $Li^0$ .** **a**, The components of an LMA before and after cycling. **b–d**, Digital photographs displaying the stability of different types of active  $Li^0$  and inactive  $Li^0$  in the biphenyl/THF solution, including a pristine LMA, Cu foils from cycled anode-free 0.5 Ah Cu/NCM811 pouch cells under 100 kPa and a current rate of 0.5C. The colour change from transparent (**b**) to dark blue (**c**) observed in the leftmost and rightmost bottles is caused by chemical metalation of exposed metallic Li by biphenyl/THF. No colour change in the other three bottles indicates that SEI-encapsulated inactive  $Li^0$  is insoluble in biphenyl/THF. After full metalation and oxidation (**d**), no residual solids are observed in the leftmost bottle that contains pure Li in the beginning. Solid residues still exist in the other four bottles, which are insoluble SEI-encapsulated inactive  $Li^0$ . **e–g**, Diagram showing the procedures for decoupling and quantifying active  $Li^0$  and inactive  $Li^0$  in cycled LMAs. **e**, Cycled LMAs were

submerged in the biphenyl/THF solution and sealed by rubber plugs in air-tight bottles. **f**, After full metalation of the active  $Li^0$ , certain mass of Li-biphenyl/THF solution was taken and subjected to thermal digestion for the quantitative measurement of the mass of the active  $Li^0$  through ICP-OES. **g**, A certain amount of deionized water was injected to the air-tight bottle to react with the inactive  $Li^0$ . The generated hydrogen was quickly sampled by using an air-tight syringe and injected to GC for quantifying inactive  $Li^0$ . Detailed descriptions about the step-by-step procedures and related calculations are in Methods. **h**, Comparison between the concentrations in biphenyl/THF solution from balance-measured results and ICP-OES quantified concentrations of commercial Li foil. The results from ICP-OES align well with the results from balance. **i**, Converted Li metal mass calibration curve as a function of the ratio of detected  $H_2$  area to Ar area from  $H_2$ -GCT; the  $H_2$  is from the reaction between Li foil and water.

performance (Fig. 4a), including the capacity retention (~95% after 50 cycles) and average Coulombic efficiency (99.85%), can remain the same among all the cells within the initial 50 cycles because of continuous compensation from the Li reservoir to recover cathode capacity. By applying the quantitative methodology, the hidden reversibility of LMAs under different pressures can be truly distinguished.

Although the capacities of these cells are almost identical within the initial 50 cycles, the mass of active  $Li^0$  and inactive  $Li^0$  acquired by ICP-OES and  $H_2$ -GCT in the same range of the cycle number differs apparently among three pressure conditions. It is observed that the remaining amount of active  $Li^0$  in the LMA is the highest under a stack pressure of 800 kPa at 0.2C after 50 cycles (Fig. 4b). Meanwhile, the mass of inactive  $Li^0$  follows the opposite trend: the formation rate of inactive  $Li^0$  at 100 kPa is the highest (Fig. 4c). All the quantified data were then fitted according to the equations to acquire the key parameters ( $R_0$ ,  $iR_0(Li^+)$ ,  $iR_0$  and  $K$ ,  $iR_0(Li^0)$  and  $K(Li^0)$ ) that describe the reversibility of LMAs. Detailed values of each parameter are listed in Supplementary Table 12. It is noted that the fitting curves are conformal with the measured data, and most points are in the 95% confidence interval (for mean values) zone (Supplementary Fig. 13), which indicates the validity of the quantification method and the related degradation model.

As shown in Fig. 4d,e, increasing stack pressure helps to improve  $R_0$  from 99.00% at 100 kPa to 99.52% at 800 kPa and the proportion of  $iR_0(Li^+)$  is reduced from 0.46% to 0.14% as the more flattened morphology of Li at higher pressure reduces the cracking possibility of SEI<sup>29,39–42</sup>. The variations of  $R_n$ ,  $iR_n(Li^0)$  and  $iR_n(Li^+)$  (Fig. 4d,e) demonstrate that the reversibility of LMAs upon cycling is jointly determined by the baseline irreversibility ( $iR_0$ ) and its related incremental coefficient ( $K$ ). Although the growth coefficients of irreversibility under different pressures at 0.2C are considered identical within the error deviations, lower  $iR_n$  is observed at 800 kPa compared with 100 kPa in Fig. 4f because of a lower  $iR_0$  of 0.33% at 800 kPa than that of 0.85% at 100 kPa. Besides,  $iR_n(Li^0)$  at 400 kPa and 800 kPa also decreases compared with that at 100 kPa, suggesting that high stack pressure mainly avoids the deterioration of electron and ion transportation due to less dendritic Li. It also demonstrates that high stack pressure ameliorates aggregation among ‘dead Li’ particles<sup>18</sup>, which enables easier electron transportation<sup>38</sup>. Long-term cycling will also be benefited from the re-utilization of inactive  $Li^0$  from the dense ‘dead Li’ layer<sup>29,42,50</sup>. Moreover, knowing the values of  $iR_0$ ,  $R_0$  and  $K$  theoretically enable failure prediction for practical LMAs. A 0.9 Ah Li/NCM811 pouch cell cycled under 0.2C and 100 kPa encounters a sudden capacity drop at the 69th cycle owing to rising ion/electron transportation resistance (Supplementary Fig. 14).

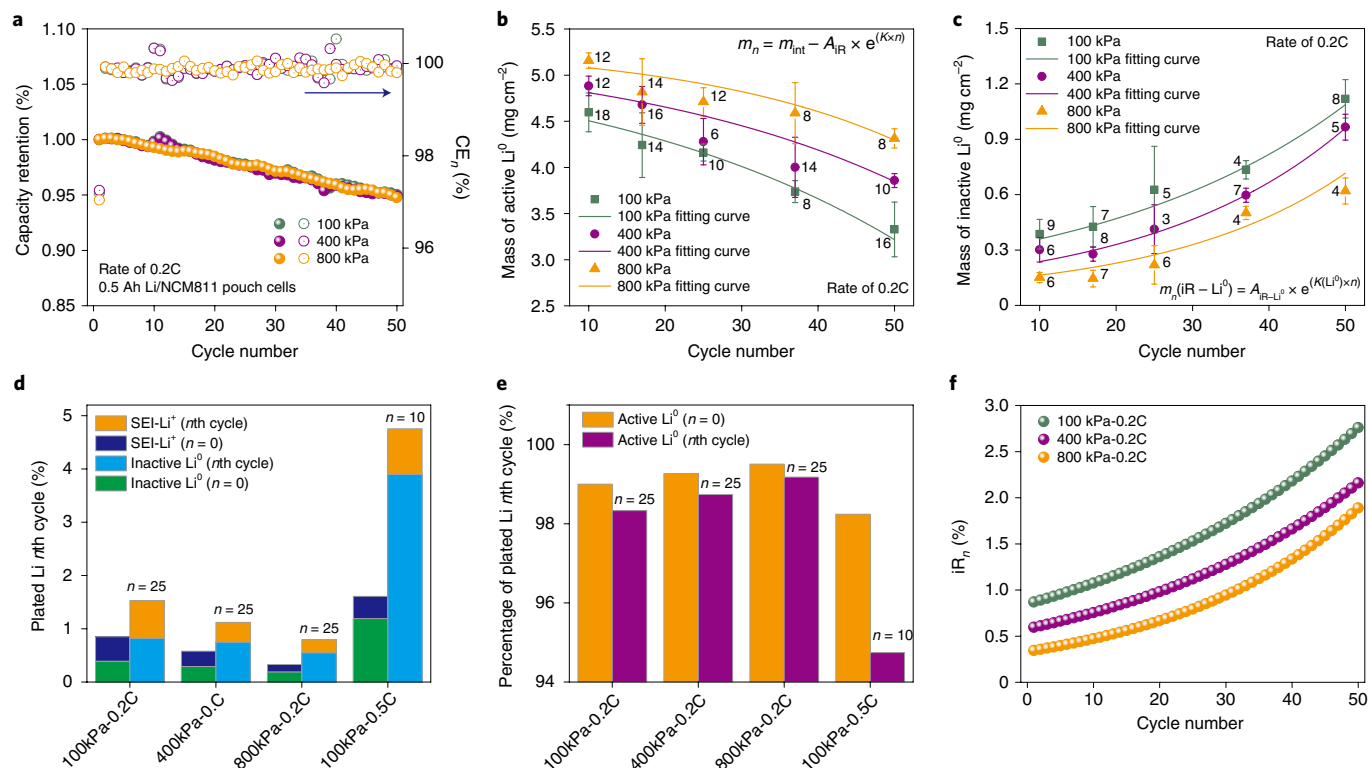


**Fig. 4 | Resolved irreversibility and reversibility from quantified results.**

**a**, The plots of capacity retention versus cycle number and  $CE_{cell}$  versus cycle number of practical 0.5 Ah Li/NCM811 pouch cells operated under different stack pressures at the rate of 0.2C. The data of the first cycle run for the activation of the cells are not included. **b, c**, The quantitatively measured masses of active  $Li^0$  (**b**) and inactive  $Li^0$  (**c**) in LMAs from the 0.5 Ah Li/NCM811 pouch cells cycled for 10, 17, 25, 37 and 50 times under different stack pressures. The numbers of data are shown near the error bars. Data are presented as mean values  $\pm$  s.d. **d, e**, The

values of  $iR_n$  and  $iR_n(Li^0)$  at the  $n$ th cycle (**d**) and of  $R_n$  at the  $n$ th cycle (**e**) resolved from the mathematical fitting results of the 0.5 Ah Li/NCM811 pouch cells under different stack pressures and rates. **f**, The plots of  $iR_n$  versus cycle number according to the resolved parameters. The corresponding data of 0.5C are shown in Supplementary Fig. 16 and Supplementary Tables 10 and 11. All the raw data of ICP-OES and  $H_2$ -GCT measurements are listed in the source data. Two separate cells and three pieces of cycled LMA disks with diameters of 14 mm taken from different locations in each cell were used for quantifications.

The thickness of the residual active  $Li^0$  is  $37 \mu m$  ( $\sim 3.0$  mg of active  $Li^0$  by theoretical estimation) as determined by a scanning electron microscope (SEM). The mathematical modelling based on the quantitative analysis results predicts that critical failure occurs after  $\sim 80$  cycles (Supplementary Fig. 15a and Supplementary Note 9), which is in good agreement with the realistic test results and reflects the practicality of this method in assessing the potential level of LMBs without long-term cycling.

### Quantitative degradation analysis of LMAs under high rates

Inactive  $Li^0$  is mainly originated from detached Li dendrites during the root-preferred stripping process; thus, quantification of inactive  $Li^0$  will offer a deeper understanding to the degradation mechanism of the LMA. The CE and capacity of the cell under 0.5C (Supplementary Fig. 16a) decay much faster than those under 0.2C (both have no constant-voltage charging process). The quantification results revealed that the mass of active  $Li^0$  drops quickly and follows the exponential decay model (Supplementary Fig. 16b). The mass of inactive  $Li^0$  increases dramatically at the rate of 0.5C, which is the main cause of rapid cell failure (Supplementary Fig. 16c). As shown in Fig. 4d,e, the values of  $iR_0$ ,  $K$ ,  $iR_0(Li^0)$ ,  $K(Li^0)$ ,  $iR_0(Li^+)$  and  $R_0$  are presented for the cells with different rates. The cell operating at the rate of 0.5C delivers a much higher  $iR_0$  of 1.61% than at the rate of 0.2C (0.85%). By applying the fitting of inactive  $Li^0$ ,  $iR_0$  are decoupled to  $iR_0(Li^0)$  and  $iR_0(Li^+)$ . Under the rate of 0.5C, the predicted increment of irreversible percentage of plated Li reaches 4.76% after only ten cycles (Supplementary Fig. 16d), and the cell suffers from fast capacity fading with a lifetime of 25 cycles.

Moreover, the irreversibility for forming SEI- $Li^+$  and inactive  $Li^0$  almost doubles compared with those at 0.2C, which explains the faster capacity decay at higher rates. As shown in Supplementary Fig. 17a, it is obvious that the exponential growth coefficient of irreversibility is dominantly governed by charging/discharge rates rather than stack pressure.

The above results of the reversibility and irreversibility of LMAs under different rates of 0.5C and 0.2C demonstrate quite different degradation modes, thus the quantitative analysis is used to uncover the structural and compositional degradation of the LMA together with qualitative morphological characterizations. In Supplementary Fig. 18a, the average standard deviations of the mass of inactive  $Li^0$  and active  $Li^0$  at 0.5C is about three times higher than that at 0.2C, implying the existence of large and unevenly distributed protrusions and pits across the entire anode after cycling at 0.5C (refs. 43–45). High values of  $K$  at 0.5C indicate that the irreversibility grows quickly due to accumulation of large quantities of ‘dead Li’ particles, which, in turn, aggravates dendritic Li growth. The total thickness of the ‘dead Li’ layer on both sides quickly exceeds  $300 \mu m$  after 25 cycles at 0.5C (Supplementary Fig. 18b), which is almost twice than that at 0.2C. A focused ion beam SEM (FIB-SEM) image of the Li anode after 25 cycles at 0.2C (Supplementary Fig. 18c,d) displays the compact accumulation state of ‘dead Li’, whereas that of 0.5C shows loosely stacking and porous morphology, which explains the much more serious thickness expanding of the LMA at higher rates that causes large polarizations due to insufficient electrolyte infiltration.

Combining quantitative analysis data and qualitative morphology characterization results, deeper understanding of compositional and structural evolution of LMAs under different rates can be established

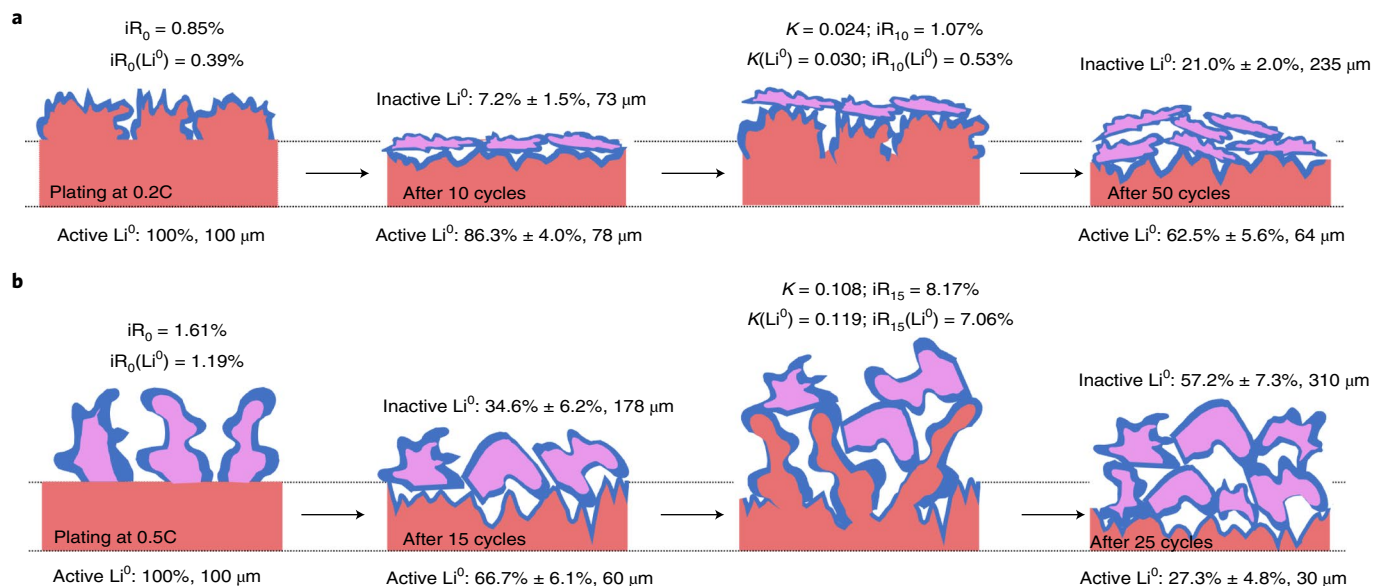


**Fig. 5 | Dynamic failure model predicted by qualitative and quantitative analysis. a,b**, The morphology evolution and the degradation processes of LMA in practical LMBs during cycling at the rates of 0.2C (a) and 0.5C (b), which are

drawn based on the quantitative analysis data and the qualitative morphological characterizations. The red and the purple regions correspond to the active  $\text{Li}^0$  and the inactive  $\text{Li}^0$ , respectively, while the blue ones correspond to the SEI.

as shown in Fig. 5a,b. At 0.2C, a low  $iR_0(\text{Li}^0)$  of 0.39% enables relatively flat Li deposition with few mossy morphologies. The quantified results confirm little fluctuation on the mass of inactive and active  $\text{Li}^0$ , which means less ‘dead Li’ and uniform stripping from the pristine LMA<sup>46–48</sup>. Thereby, parasitic effects from irreversible Li will be slowly initiated as reflected by a small growth coefficient  $K$  of 0.024. The values of  $iR_{10}(\text{Li}^0)$  and  $iR_{10}$  equal to 0.53% and 1.07%, respectively, showing little increment from the baseline ( $iR_0(\text{Li}^0)$  and  $iR_0$ ) after ten cycles. This represents compact agglomeration of ‘dead Li’, predicting that continuous stripping/plating of Li will be hardly disturbed by concentration polarization. In contrast, increasing the rate to 0.5C induces serious inhomogeneity of charge distribution on the LMA, resulting in porous interphase growth over the anode, which is responsible for the high  $iR_0(\text{Li}^0)$  of 1.19% and  $iR_0(\text{Li}^+)$  of 0.42%. Thus massive and fast growth of dendritic Li continuously occurs, which continually breaks SEI to consume active  $\text{Li}^0$  (refs. 35,46). A large amount of inactive  $\text{Li}^0$  particles are quickly formed by the detached dendritic Li protrusions, while the compensation of Li from the LMA to the inventory loss of the cathode in the stripping process produces large and random pits in the LMA, giving rise to large standard deviations of the quantification results<sup>32</sup>. Highly porous and thick ‘dead Li’ layers result in serious mass transportation issues and insufficient electrolyte infiltration (Supplementary Fig. 19 and Supplementary Note 10), which induce problematic exhaustion of Li ions near anode interface and hindrance of electron transport. Thereafter, severe cumulative parasitic effects as reflected by a high baseline irreversibility of 1.61% and a high exponential growth coefficient of 0.108 cause extremely unstable plating behaviour of Li that induces a large amount of Li dendrites, giving rise to a high  $iR_{15}(\text{Li}^0)$  of 7.06% and  $iR_{15}$  of 8.17% only after 15 cycles. Meanwhile, heavily charged locations will dynamically move to a more curved surface to initiate new electron concentrated areas that intensify the inhomogeneity of Li plating/stripping<sup>49</sup>. Finally, fast exhaustion of active  $\text{Li}^0$  results in total failure of the cell. The much worse rate capability of LMB pouch cells than that of coin cells presented in most research works strongly suggests that the degradation behaviour of LMAs in practical pouch cells cannot be simply learned from that in coin cell setups. These findings suggest that extensive optimization of LMAs is needed for long cycle life at high current densities, which is essential to enable high-energy density LMBs with acceptable rate capability for practical applications.

## Conclusions

In summary, an analytical method is proposed to quantitatively distinguish active  $\text{Li}^0$  from inactive ones in cycled LMAs, which enables the decoupling of the proportions of real reversibility and irreversibility of practical LMAs. A set of key parameters is identified to describe the hidden behaviour of Li plating/stripping in practical cells. Applying this method on practical Ah-level pouch cells reveals the differences in reversibility of Li plating/stripping under different conditions, including the stack pressure and charge/discharge rate. Moreover, combining with morphological characterization, the structural evolution and degradation process of LMAs in practical LMBs can be revealed in detail in a quantitative way. We believe that this method will become a powerful tool to deeply understand the electrochemical behaviour of LMAs and to assess the true reversibility of LMBs, which is essential to the development of high-performance LMBs.

## Methods

### Materials

Tetrahydrofuran (THF, anhydrous, purity  $\geq 99.9\%$ , inhibitor-free) and biphenyl (purity  $\geq 99.0\%$ ) were purchased from Sigma-Aldrich. Before use, all the THF solvent was handled by molecular sieve to remove the residual water. The electrolyte was composed of 1.0 M  $\text{LiPF}_6$  in fluoroethylene carbonate/ethyl methyl carbonate (in volumetric ratio 1:5). Li foils of 45  $\mu\text{m}$  and 100  $\mu\text{m}$  were employed as LMAs. NCM811 cathodes were kindly provided by Ningbo FuLi Battery Material Technology.

### Pouch cell assembly and electrochemical tests

To fabricate the practical LMBs, 45  $\mu\text{m}$  Li foils and 100  $\mu\text{m}$  Li foils were employed as LMAs (4.7 cm  $\times$  5.7 cm, excluding the tap area) to reach the designed N/P ratios. The Z-shape stacking cell geometry is shown in Supplementary Fig. 3. Three pieces of double-coated NCM811 (areal loading of 20.0 mg  $\text{cm}^{-2}$  on one side) with tailor-made dimensions (4.3 cm  $\times$  5.3 cm) were employed as the cathodes. The cells were encapsulated in aluminium packing foil (areal loading of 3.27 mg  $\text{cm}^{-2}$ ) by hot pressing, followed by electrolyte injection with the dosage of 4.0 g  $\text{Ah}^{-1}$  and connection of the taps (Ni and Al strips) using a laser welding machine. Before electrochemical tests, certain stack pressures were applied on these pouch cells (Supplementary Fig. 4a,b) by using homemade pressurizing equipment and cell holders (Supplementary

Fig. 4c,d). Pouch cells with certain stack pressures in cell holders were connected to an LANHE-CT2001A system (Jinnuo Wuhan). For the Li/NCM811 pouch cells, the charge/discharge rates were set at 0.2C and 0.5C (1C equals 600 mA) between the voltage of 2.6 V and 4.3 V. The procedures for activation of the fresh pouch cell were performed under 400 kPa and room temperature; the cell was first charged at 0.05C for 30 min and then charged at 0.1C to 4.3 V, rested for 10 mins, then was discharged at 0.1C to 2.6 V. Detailed parameters for the assembly of practical pouch cells could also be seen in previous work<sup>9</sup>.

### Characterizations

The inductively coupled plasma-optical emission spectrometry (ICP-OES, Optima 2100) was employed in the ICP-OES method. The gas chromatography (Agilent Technologies 7890B) was used to quantify the amount of hydrogen. SEM (Hitachi S-4800 field emission scanning electron microscope) and FIB-SEM (Auriga produced by Carl Zeiss) was used to characterize the morphology of LMAs after cycling.

### Additional mathematical equations

In practical LMBs, Li resources are extracted from the cathode and plated as metallic Li during the charging process and undergoing a reverse way during the discharging process. Irreversible Li loss is inevitable during charging/discharging. In the discharging process, sufficient Li inventory in the LMA will compensate for the loss of cathode in the previous cycle. Before the Li inventory in the LMA was exhausted, the CE measured by the electrochemical charge/discharge curves is closely related to the irreversible Li loss of cathode ( $CiE_n$ ), only at stable cycling performances without evident overcharge or electrolyte decomposition problems. Thus,  $CiE_n$  can be directly acquired from CE of the cell ( $CE_n$ ) as follows.

$$CiE_n = 100\% - CE_n \quad (9)$$

The total Li amount utilized in one charge/discharge cycle in an LMB is composed of reversible Li (active  $Li^0$ ), Li species in SEI- $Li^+$ , inactive  $Li^0$  encapsulated by SEI and irreversible Li loss in the cathode, as shown in Fig. 1b; therefore

$$R_n(Li^0) + iR_n(Li^0) + iR_n(Li^+) + CiE_n = 100\% \quad (10)$$

$R_n$  and  $iR_n$  represent the reversibility and irreversibility of Li plating during the charging process of the  $n$ th cycle. To clearly demonstrate the mathematical relationship between cycle number and content of active  $Li^0$ , several parameters are defined in Table 1. Cell balance is referred as the ratio of anode capacity to cathode capacity (N/P ratio);  $m_{int}$  ( $mg\ cm^{-2}$ ) is defined as the initial areal mass of pristine LMA (5.34  $mg\ cm^{-2}$  for the mathematical fitting as indicated in Supplementary Table 8 and Supplementary Note 7) and  $m_n$  ( $mg\ cm^{-2}$ ) as the areal mass of active  $Li^0$  in cycled LMAs after  $n$  cycles. The corresponding total Li areal mass ( $m_{Li,Cat}$ ,  $mg\ cm^{-2}$ ) extracted from the cathode during the charging process can be calculated using the following equation.

$$m_{Li,Cat} = \frac{m_{Cat} \times C_{Cat}}{C_{LMA}} = \frac{m_{int}}{\left(\frac{N}{P}\right)} \quad (11)$$

Assuming that the irreversibility of Li plating during charging keeps constant without considering the accumulative effects, that is

$$\frac{d(iR_n)}{dn} = 0 \quad (12)$$

Thus,  $iR_n$  equals to  $iR_0$ , and the relationship between areal mass of residual active  $Li^0$  and cycle number ( $n$ ) is expressed in equation (13).

$$m_n = m_{int} - \frac{m_{int}}{\left(\frac{N}{P}\right)} \times iR_0 \times n \quad (13)$$

In fact, as described in the main text, irreversibility of LMB undergoes an exponential growth due to continuous formation and agglomeration of irreversible Li on the surface of the anode, causing the deviation of  $iR_n$  from the initial baseline  $iR_0$ . For the exponential growth mode of  $iR_n$ , a coefficient  $K$  is employed to represent the growth rate of irreversibility (including inactive  $Li^0$  and SEI- $Li^+$ ) as described in equation (2). Equation (5) can also be expressed as the relationship between the retention ratio of active  $Li^0$  and the cycle number as expressed in equation (14).

$$\frac{m_n}{m_{int}} = 1 - \frac{iR_0 \times iCE_{cell}}{\left(\frac{N}{P}\right) \times K} \times e^{K \times n} \quad (14)$$

To describe the variation of the inactive  $Li^0$  during cycling, we assume the evolution of inactive  $Li^0$  follows the exponential growth law, thus, the relationship between  $iR_n(Li^0)$ ,  $K(Li^0)$  and  $n$  is expressed as follows.

$$iR_n(Li^0) = iR_0(Li^0) \times e^{K(Li^0) \times n} \quad (15)$$

The sum of accumulated areal mass of inactive  $Li^0$  ( $m_n(iR-Li^0)$ ) after  $n$  cycles is expressed in equations (16) and (17), according to previous mathematical hypothesis and calculation process.

$$m_n(iR-Li^0) = \frac{m_{int}}{\left(\frac{N}{P}\right)} \times iR_0(Li^0) \times [e^{K(Li^0) \times 1} + e^{K(Li^0) \times 2} + \dots + e^{K(Li^0) \times n}] \quad (16)$$

$$\frac{m_n(iR-Li^0)}{m_{int}} = \frac{iR_0(Li^0)}{\left(\frac{N}{P}\right) \times K(Li^0)} \times e^{K(Li^0) \times n} \quad (17)$$

For more accurate quantification of the values of reversibility and irreversibility, the initial Coulombic efficiency ( $iCE_{cell}$ ) of the cathode should also be considered for mathematical fitting. We introduce  $iCE_{cell}$  in equations (4) and (5) to calibrate the calculation of  $iR_0$  and  $K$ . The  $CE_{cell}$  applied in the equations equals to 93.67% according to the results in Supplementary Table 1.

### Analytical methodology

Detailed procedures for quantitative analysis of the active  $Li^0$  and inactive  $Li^0$  in cycled LMAs are described as follows.

Electrode disks (14 mm in diameter) along with a separator obtained by punching different locations in each cycled LMA taken out from the pouch cells (Supplementary Fig. 5) were rinsed for three times with THF (8–10 ml) to remove the residual LiPF<sub>6</sub> and then dried in an Ar-filled glove box before quantitative measurement (Supplementary Table 2 and Supplementary Note 1). Anode-free coin cells (Li/Cu cells) were also tested to characterize the stability of SEI against biphenyl/THF; however, our results demonstrated the residues on Cu foil obtained from Li/Cu coin cells did not seem to be pure inactive  $Li^0$ . Consequently, all analytical procedures were performed on cycled LMAs from Ah-level pouch cells. It is important to stress that not enough data have been obtained to verify whether this method can also be effectively applied for the cycled LMAs in coin cells.

Biphenyl and THF were selected as the reagents for chemical metalation, which can dissolve metallic Li for the purpose of separating inactive  $Li^0$  and active  $Li^0$ . There is a charge-transfer process between lithium and biphenyl followed by Li coordination with ether oxygens in THF. The reaction equation of biphenyl and metallic Li is shown in Supplementary Fig. 7. We added 8–10 ml of biphenyl/THF (with 6.0 wt% of biphenyl) into the air-tight glass bottle containing one disk sample obtained in the first step to dissolve the active  $Li^0$ . After punching the cycled LMA to a circular piece (diameter of 14 mm), the fresh punching boundaries of the residual bulk Li (active  $Li^0$ ) were exposed without SEI covering. The biphenyl/THF solution contacts with active

$\text{Li}^0$  at the fresh punching boundaries. At the same time, the 'dead Li' particles near the punching boundary would be broken and then dissolved by biphenyl/THF. Although the thickness of the porous Li layer is 300  $\mu\text{m}$ , the size of the porous Li particles, more likely as dead dendrites, is smaller than 50  $\mu\text{m}$ , according to the SEM images in Supplementary Figs. 20–27. If all 50  $\mu\text{m}$ -size dead Li at the boundaries are inactive  $\text{Li}^0$  and got damaged by the punching process, it can be calculated that the mass ratio of the damaged inactive  $\text{Li}^0$  at the boundaries to total inactive  $\text{Li}^0$  in the circular piece is 1.42%. For a specific anode with 200  $\mu\text{m}$  thick 'dead Li' layer after cycling under 0.5C and 100 kPa, the maximum quantified mass of inactive  $\text{Li}^0$  is 5 mg, thus the loss of inactive  $\text{Li}^0$  is -0.071 mg, which is close to the machine's limit of quantification (LOQ of ICP-OES is 0.074 mg). Thus, we think the relatively low mass ratio of the damaged inactive  $\text{Li}^0$  at the boundaries would not interfere with the quantification results by ICP-OES. After a certain period (36–48 h) at 25 °C, the mass of the whole Li-biphenyl/THF solution was recorded as  $m_{\text{target}}$  (gram as the unit). A given volume of Li-biphenyl/THF solution (1 or 2 ml) was then quickly sampled. To ensure the accuracy of the results measured by ICP-OES, the sampled liquid was quickly injected to pure THF ( $m_{\text{dilute}}$ , gram as the unit) and sealed. The whole mass of Li-biphenyl/THF after diluting was precisely weighed using a microbalance and recorded as  $m_{\text{solution}}$  (gram as the unit). Each sampled solution was then used for two parallel digestions; the mass of the digestion liquid was precisely weighed using a microbalance and recorded as  $m_{\text{digestion}}$  (gram as the unit). After full evaporation of THF from samples for digestions, Li-biphenyl/THF solutions were then subjected to chemical digestion to break organic Li-biphenyl and THF to water-soluble substances for ICP-OES. The digestion procedures were carried out by hydrothermally heating the solution with  $\text{HNO}_3$  (4.5 ml),  $\text{H}_2\text{O}_2$  (0.75 ml) and  $\text{HClO}_4$  (0.75 ml) at 180 °C for 4 h in an autoclave after pre-heating for 30 min at 110 °C under air atmosphere. The aqueous solution after the digestion procedure was carefully collected and diluted with deionized water in a volumetric flask of  $V_{\text{flask}}$  of 25.0 ml, which was then subjected to ICP-OES measurement ( $C_{\text{ICP-OES}}$ ,  $\text{mg l}^{-1}$  as the unit) to quantify the concentration of Li in the original Li-biphenyl/THF solution. The equation for calculating the mass of active Li ( $m_{\text{active Li}}$ , mg as the unit) is expressed in equation (18).

$$m_{\text{active Li}} = \frac{C_{\text{ICP-OES}} \times m_{\text{solution}} \times m_{\text{target}} \times V_{\text{flask}}}{1,000 \times (m_{\text{solution}} - m_{\text{dilute}}) \times m_{\text{digestion}}} \quad (18)$$

A given amount (2.0 ml) of deionized water was injected into the same air-tight bottle used earlier by a 5.0 ml air-tight syringe (Supplementary Fig. 6b). The generated gas was quickly sampled using a 25 ml air-tight syringe (Supplementary Fig. 6c), followed by the injection into a vacuum and air-tight Al foil packing bag (Supplementary Fig. 6d). The gas in the bag was then injected to the GC equipment for quantifying the mass of the inactive  $\text{Li}^0$ . Hydrogen is the only gas generated by the reaction of pure Li with water. But as shown in Supplementary Fig. 11d, the SEI formed in cycled LMAs will also react with water to release  $\text{CO}_2$ ,  $\text{CH}_4$ ,  $\text{C}_2\text{H}_4$  and  $\text{C}_2\text{H}_6$ . The generation of additional gases besides hydrogen will affect the molar ratio of  $\text{H}_2$  in the sample gases, interfering the peak area related to hydrogen for further quantitative measurement of hydrogen. Therefore, the calibration curve (such as the curve in Supplementary Fig. 12a and Supplementary Note 5) established using pure Li foil with known weight is not able to accurately measure the inactive Li from cycled LMAs. Fortunately, we found that argon, which has a fixed content amount in all samples, could be used as a reference gas for internal calibration. After sealing in the Ar-filled glove box, the volume of Ar in the gas sample is kept unchanged during the entire measuring process. The integral area of the peaks related to  $\text{H}_2$  ( $S_{\text{hydrogen-test}}$ ) and that of Ar ( $S_{\text{argon-test}}$ ) in gas chromatography–mass spectrometry (GC-MS) spectra were automatically calculated by the software, respectively. Therefore, we could use the molar ratio of  $\text{H}_2/\text{Ar}$  instead of the ratio of  $\text{H}_2/\text{all gases}$  for quantitative analysis. Namely,

during the whole  $\text{H}_2$ -GCT process, the mole of  $\text{H}_2$  ( $n_{\text{hydrogen}}$ ), the mole of Ar ( $n_{\text{argon}}$ ), the integral area of  $\text{H}_2$  ( $S_{\text{hydrogen}}$ ) and the integral area of Ar ( $S_{\text{argon}}$ ) follow equation (19)

$$\frac{n_{\text{hydrogen}}}{n_{\text{argon}}} = \frac{S_{\text{hydrogen}}}{S_{\text{argon}}} \times C \quad (19)$$

where  $C$  represents the constant between molar ratio and integral area in  $\text{H}_2$ -GCT. Five calibrating gases including different ratios of hydrogen, nitrogen and argon are used (detailed ratios are listed in Supplementary Table 6) to calculate  $C$ . The GC-MS spectra of different calibrating gases are shown in Supplementary Fig. 12d.

Despite that constant  $C$  can be acquired by applying different calibrating gases, actually, the exact mole of Ar is not clear in the bottle. Thus, pure Li foils with known masses and pure THF with the same volume as that of the residual liquid are employed as the reference to characterize the mole of Ar here.

For pure Li, the equation is listed below.

$$\frac{n_{\text{hydrogen}}}{n_{\text{argon}}} = \frac{n_{\text{pure Li}}}{n_{\text{argon-pure Li}}} = \frac{S_{\text{hydrogen-pure Li}}}{S_{\text{argon-pure Li}}} \times C \quad (20)$$

For the cycled LMA sample, the equation is listed below.

$$\frac{n_{\text{hydrogen}}}{n_{\text{argon}}} = \frac{n_{\text{active Li}}}{n_{\text{argon-test}}} = \frac{S_{\text{hydrogen-test}}}{S_{\text{argon-test}}} \times C \quad (21)$$

As the volume of Ar remains unchanged between the reference samples and the tested samples, the molar ratio of  $\text{H}_2$  to Ar in two cases is proportional to the mass ratio of pure Li foil to the inactive Li in cycled LMAs. Thus, the calibrated and modified calculation equation for precise measurement of the mass of inactive Li is expressed in equation (22), where  $S_{\text{argon-pure Li}}$ ,  $S_{\text{hydrogen-pure Li}}$  and  $m_{\text{pure Li}}$  are the parameters with known average values according to the calibration experiments.

$$m_{\text{active Li}} = \frac{S_{\text{hydrogen-test}}}{S_{\text{argon-test}}} \times \frac{S_{\text{argon-pure Li}}}{S_{\text{hydrogen-pure Li}}} \times m_{\text{pure Li}} \quad (22)$$

The limit of detection and LOQ of ICP-OES is 0.026 mg and 0.074 mg, respectively, and the limit of detection and LOQ of  $\text{H}_2$ -GCT is 0.056 mg and 0.094 mg, respectively (Supplementary Table 7 and Supplementary Note 6).

## Data availability

The datasets analysed and generated during the current study are included in the paper and its Supplementary Information. Source data are provided with this paper.

## References

- Liu, J. et al. Pathways for practical high-energy long-cycling lithium metal batteries. *Nat. Energy* **4**, 180–186 (2019).
- Albertus, P., Babinec, S., Litzelman, S. & Newman, A. Status and challenges in enabling the lithium metal electrode for high-energy and low-cost rechargeable batteries. *Nat. Energy* **3**, 16–21 (2017).
- Chen, S. et al. Critical parameters for evaluating coin cells and pouch cells of rechargeable Li-metal batteries. *Joule* **3**, 1094–1105 (2019).
- Chen, S., Dai, F. & Cai, M. Opportunities and challenges of high-energy lithium metal batteries for electric vehicle applications. *ACS Energy Lett.* **5**, 3140–3151 (2020).
- Fang, C., Wang, X. & Meng, Y. S. Key issues hindering a practical lithium-metal anode. *Trends Chem.* **1**, 152–158 (2019).
- Zhang, X., Yang, Y. & Zhou, Z. Towards practical lithium-metal anodes. *Chem. Soc. Rev.* **49**, 3040–3071 (2020).

7. Weber, R. et al. Long cycle life and dendrite-free lithium morphology in anode-free lithium pouch cells enabled by a dual-salt liquid electrolyte. *Nat. Energy* **4**, 683–689 (2019).
8. Huang, C.-J. et al. Decoupling the origins of irreversible Coulombic efficiency in anode-free lithium metal batteries. *Nat. Commun.* **12**, 1452 (2021).
9. Deng, W. et al. Competitive solvation-induced concurrent protection on the anode and cathode toward a 400 Wh kg<sup>-1</sup> lithium metal battery. *ACS Energy Lett.* <https://doi.org/10.1021/acseenergylett.0c02351> (2020).
10. Deng, W., Zhou, X., Fang, Q. & Liu, Z. Microscale lithium metal stored inside cellular graphene scaffold toward advanced metallic lithium anodes. *Adv. Energy Mater.* **8**, 1703152 (2018).
11. Kim, M. S. et al. Langmuir–Blodgett artificial solid-electrolyte interphases for practical lithium metal batteries. *Nat. Energy* **3**, 889–898 (2018).
12. Adams, B. D., Zheng, J., Ren, X., Xu, W. & Zhang, J. G. Accurate determination of Coulombic efficiency for lithium metal anodes and lithium metal batteries. *Adv. Energy Mater.* **8**, 1702097 (2018).
13. Xiao, J. et al. Understanding and applying Coulombic efficiency in lithium metal batteries. *Nat. Energy* **5**, 561–568 (2020).
14. Holtstiege, F., Wilken, A., Winter, M. & Placke, T. Running out of lithium? A route to differentiate between capacity losses and active lithium losses in lithium-ion batteries. *Phys. Chem. Chem. Phys.* **19**, 25905–25918 (2017).
15. Niu, C. et al. Balancing interfacial reactions to achieve long cycle life in high-energy lithium metal batteries. *Nat. Energy* **6**, 723–732 (2021).
16. Paul, P. P. et al. A review of existing and emerging methods for lithium detection and characterization in Li-ion and Li-metal batteries. *Adv. Energy Mater.* **11**, 2100372 (2021).
17. Fang, C. et al. Quantifying inactive lithium in lithium metal batteries. *Nature* **572**, 511–515 (2019).
18. Chen, K.-H. et al. Dead lithium: mass transport effects on voltage, capacity, and failure of lithium metal anodes. *J. Mater. Chem. A* **5**, 11671–11681 (2017).
19. Lu, D. et al. Failure mechanism for fast-charged lithium metal batteries with liquid electrolytes. *Adv. Energy Mater.* **5**, 1400993 (2015).
20. Xu, S., Chen, K.-H., Dasgupta, N. P., Siegel, J. B. & Stefanopoulou, A. G. Evolution of dead lithium growth in lithium metal batteries: experimentally validated model of the apparent capacity loss. *J. Electrochem. Soc.* **166**, A3456 (2019).
21. Chandrashekar, S. et al. <sup>7</sup>Li MRI of Li batteries reveals location of microstructural lithium. *Nat. Mater.* **11**, 311–315 (2012).
22. Gunnarsdóttir, A. B., Amanchukwu, C. V., Menkin, S. & Grey, C. P. Noninvasive in situ NMR study of ‘dead lithium’ formation and lithium corrosion in full-cell lithium metal batteries. *J. Am. Chem. Soc.* **142**, 20814–20827 (2020).
23. Aryanfar, A., Brooks, D. J., Colussi, A. J. & Hoffmann, M. R. Quantifying the dependence of dead lithium losses on the cycling period in lithium metal batteries. *Phys. Chem. Chem. Phys.* **16**, 24965–24970 (2014).
24. McShane, E. J. et al. Quantification of inactive lithium and solid–electrolyte interphase species on graphite electrodes after fast charging. *ACS Energy Lett.* **5**, 2045–2051 (2020).
25. Janakiraman, U., Garrick, T. R. & Fortier, M. E. Lithium plating detection methods in Li-ion batteries. *J. Electrochem. Soc.* **167**, 160552 (2020).
26. Hsieh, Y.-C. et al. Quantification of dead lithium via in situ nuclear magnetic resonance spectroscopy. *Cell Rep. Phys. Sci.* **1**, 100139 (2020).
27. Gunnarsdóttir, A. B., Vema, S., Menkin, S., Marbella, L. E. & Grey, C. P. Investigating the effect of a fluoroethylene carbonate additive on lithium deposition and the solid electrolyte interphase in lithium metal batteries using in situ NMR spectroscopy. *J. Mater. Chem. A* **8**, 14975–14992 (2020).
28. Xiang, Y. et al. Quantitatively analyzing the failure processes of rechargeable Li metal batteries. *Sci. Adv.* **7**, eabj3423 (2021).
29. Fang, C. et al. Pressure-tailored lithium deposition and dissolution in lithium metal batteries. *Nat. Energy* **6**, 987–994 (2021).
30. Bao, W. et al. Quantifying lithium loss in amorphous silicon thin-film anodes via titration-gas chromatography. *Cell Rep. Phys. Sci.* **2**, 100597 (2021).
31. Zheng, J. et al. Physical orphaning versus chemical instability: is dendritic electrodeposition of Li fatal? *ACS Energy Lett.* **4**, 1349–1355 (2019).
32. Niu, C. et al. High-energy lithium metal pouch cells with limited anode swelling and long stable cycles. *Nat. Energy* **4**, 551–559 (2019).
33. Hu, Z. et al. Self-adaptive 3D skeleton with charge dissipation capability for practical Li metal pouch cells. *Nano Energy* **93**, 106805 (2022).
34. Gao, N. et al. Fast diagnosis of failure mechanisms and lifetime prediction of Li metal batteries. *Small Methods* **5**, 2000807 (2021).
35. Wood, K. N., Noked, M. & Dasgupta, N. P. Lithium metal anodes: toward an improved understanding of coupled morphological, electrochemical, and mechanical behavior. *ACS Energy Lett.* **2**, 664–672 (2017).
36. Wang, L. et al. Identifying the components of the solid–electrolyte interphase in Li-ion batteries. *Nat. Chem.* **11**, 789–796 (2019).
37. Nie, M. et al. Lithium ion battery graphite solid electrolyte interphase revealed by microscopy and spectroscopy. *J. Phys. Chem. C* **117**, 1257–1267 (2013).
38. Hirota, N. Electron paramagnetic resonance studies of ion pairs. Structures and equilibria in alkali metal naphthalenide and anthracenide. *J. Am. Chem. Soc.* **90**, 3603–3611 (1968).
39. Zhang, X. et al. Rethinking how external pressure can suppress dendrites in lithium metal batteries. *J. Electrochem. Soc.* **166**, A3639–A3652 (2019).
40. Yin, X. et al. Insights into morphological evolution and cycling behaviour of lithium metal anode under mechanical pressure. *Nano Energy* **50**, 659–664 (2018).
41. Louli, A. J. et al. Exploring the impact of mechanical pressure on the performance of anode-free lithium metal cells. *J. Electrochem. Soc.* **166**, A1291–A1299 (2019).
42. Monroe, C. & Newman, J. The impact of elastic deformation on deposition kinetics at lithium/polymer interfaces. *J. Electrochem. Soc.* <https://doi.org/10.1149/1.1850854> (2005).
43. Wood, K. N. et al. Dendrites and pits: untangling the complex behavior of lithium metal anodes through operando video microscopy. *ACS Cent. Sci.* **2**, 790–801 (2016).
44. Brissot, C., Rosso, M., Chazalviel, J.-N. & Lascaud, S. Dendritic growth mechanisms in lithium/polymer cells. *J. Power Sources* **81**, 925–929 (1999).
45. Chen, X. R. et al. A diffusion-reaction competition mechanism to tailor lithium deposition for lithium-metal batteries. *Angew. Chem. Int. Ed.* **132**, 7817–7821 (2020).
46. Bai, P., Li, J., Brushett, F. R. & Bazant, M. Z. Transition of lithium growth mechanisms in liquid electrolytes. *Energy Environ. Sci.* **9**, 3221–3229 (2016).
47. Liu, Y. et al. Insight into the critical role of exchange current density on electrodeposition behavior of lithium metal. *Adv. Sci.* **8**, 2003301 (2021).
48. Yamaki, J.-i. et al. A consideration of the morphology of electrochemically deposited lithium in an organic electrolyte. *J. Power Sources* **74**, 219–227 (1998).

49. Wang, S. H. et al. Stable Li metal anodes via regulating lithium plating/stripping in vertically aligned microchannels. *Adv. Mater.* **29**, 1703729 (2017).
50. Liu, F. et al. Dynamic spatial progression of isolated lithium during battery operations. *Nature* **600**, 659–663 (2021).

## Acknowledgements

This work was supported by National Natural Science Foundation of China (grant number 52001320, 51872305), ‘Lingyan’ Research and Development Plan of Zhejiang Province (grant number 2022C01071) and China Postdoctoral Science Foundation funded project (grant number 2019TQ0331, 2019M662123). Y.S.M. acknowledges funding support from the Zable Endowed Chair of Energy Technology and the Sustainable Power & Energy Center of UC San Diego. W.D. thanks F. Zhao for helpful discussions about the work; Q. Guo for discussions about mathematical equations; Z. Jiang, Q. Han, W. Fang and J. Wang for their help on the pouch cell assembly and tests; and A. Cao, Y. Yu, S. Liu and H. Li for their help on ICP-OES and GC characterizations. W.D. thanks Y. Han for help with GC analysis, Y. Li for Ar-BET characterizations and K. Shen for ICP-OES analysis from the testing centre of NIMTE, CAS.

## Author contributions

W.D., X.Z., Y.S.M. and Z.L. conceived the concept and the project. W.D. and W.B. performed the analytical procedures and data analysis. W.D. and X.Y. performed the ICP-OES characterizations. W.D., Z.H. and B.H. assembled and tested the pouch cells. W.D., W.B., X.Z., B.Q., Y.S.M. and Z.L. wrote and revised the manuscript. All authors discussed the results and reviewed the manuscript.

## Competing interests

The authors declare no competing interests.

## Additional information

**Supplementary information** The online version contains supplementary material available at <https://doi.org/10.1038/s41560-022-01120-8>.

**Correspondence and requests for materials** should be addressed to Xufeng Zhou, Ying Shirley Meng or Zhaoping Liu.

**Peer review information** *Nature Energy* thanks the anonymous reviewers for their contribution to the peer review of this work.

**Reprints and permissions information** is available at [www.nature.com/reprints](http://www.nature.com/reprints).

**Publisher’s note** Springer Nature remains neutral with regard to jurisdictional claims in published maps and institutional affiliations.

Springer Nature or its licensor holds exclusive rights to this article under a publishing agreement with the author(s) or other rightsholder(s); author self-archiving of the accepted manuscript version of this article is solely governed by the terms of such publishing agreement and applicable law.

© The Author(s), under exclusive licence to Springer Nature Limited 2022